Journal of Materials Chemistry A

ROYAL SOCIETY OF CHEMISTRY

PAPER

View Article Online
View Journal

Cite this: DOI: 10.1039/d2ta08410d

Synthesis of metal cation doped nanoparticles for single atom alloy catalysts using spontaneous cation exchange†

Xiangyun Xiao, ‡[ab] Sungsu Kang,‡[cd] Seokhyun Choung, ‡[e] Jeong Woo Han, *[e] Jungwon Park *[cdfg] and Taekyung Yu *[a]

Ion exchange is a chemical reaction in which the ionic components of a solid parent material are exchanged with other ions. It often happens in metal chalcogenide and ionic metal oxide crystals, which are composed of cation and anion constituents. Here, we discovered that the cations in a solution spontaneously exchange with the constituent atoms in metal nanoparticles, forming cation-doped metal nanoparticles. Owing to charge–charge repulsion, the cations are atomically dispersed without aggregating in the nanoparticles that act as single-atom catalysts. The prepared PdRu and PdCe catalysts exhibited remarkable activity for methanol oxidation reaction and hydrogen evolution reaction, in which the Ru and Ce cations serve as active sites. This cation exchange reaction provides a specific tool to synthesize cation single atom catalysts in mild conditions that cannot be obtained *via* other synthetic methods and will spawn applications like photodynamic therapy, chemical sensing, and devices.

Received 28th October 2022
Accepted 5th January 2023

DOI: 10.1039/d2ta08410d

rsc.li/materials-a

Introduction

Ion exchange is a chemical reaction in which ions in a solid parent material are exchanged with other ions.[1] Usually, incoming ions expel the ions in the host material outward by solid-state diffusion, which is often accelerated by vacancies and interstitial sites.[2] Because of smaller ionic radii and higher diffusivities, cations are more rapidly exchanged than anions. Additionally, because the overall particle morphology is maintained in cation exchange, this method is advantageous for preparing ionic nanocrystals with controlled morphology.[3] Moreover, cation exchange enables a wide range of materials to be synthesized including oxides, chalcogenides, and halides[4–7] as well as complex nanostructures such as alloys,[8] core/shells[9] and hollow[10] nanoparticles, and segmented architectures[11] by rapid and low-temperature cation-to-cation transformations.[12] However, ion exchange has been limited to particular materials such as metal chalcogenide and ionic metal oxide crystals composed of cation and anion constituents.[13,14] Here, we discovered a cation-exchange phenomenon in which zero-valent metallic atoms in the metal nanoparticles are replaced by incoming cations in an acidic solution. The vacancies of the launched metal atoms were doped by cations with a smaller radius and caused lattice shrinkage. This cation exchange prominently exhibits selective exchange between metal atoms and cations and forms cation-doped metal nanoparticles. In the present studies, we confirmed that metal cations, including Ru^{3+}, Ce^{3+}, Eu^{3+}, Fe^{3+}, and Mn^{2+}, exchange with metallic Pd or Au atoms in the nanoparticles.

Single-atom alloys (SAAs) are a type of single-site catalysts, including reactive metal dopants atomically isolated and alloyed into the surface of a less reactive metal host.[15] SAAs have emerged as a frontier in heterogeneous catalysis because of their specific electronic structure driven by uniform active sites, peculiar geometry, and the possibility of maximum atomic utilization.[16–18] Despite the outstanding catalytic performance of SAAs in many reactions, SAAs are difficult to synthesize because the reactive metal atoms easily agglomerate due to their high surface energy.[19] Therefore, previously reported SAA catalysts contain a large portion of nanoparticles and nanoclusters added to single-atom sites. Furthermore, conventional SAA synthesis methods typically require complicated and harsh

[a]Department of Chemical Engineering, College of Engineering, Integrated Engineering Major, Kyung Hee University, Yongin 17140, Korea. E-mail: tkyu@khu.ac.kr

[b]Faculty of Materials Science and Engineering/Institute of Technology for Carbon Neutrality, Shenzhen Institute of Advanced Technology (SIAT), Chinese Academy of Sciences (CAS), Shenzhen, 518055 P. R. China

[c]School of Chemical and Biological Engineering, Institute of Chemical Process, Seoul National University, Seoul 08826, South Korea. E-mail: jungwonpark@snu.ac.kr

[d]Center for Nanoparticle Research, Institute for Basic Science (IBS), Seoul 08826, South Korea

[e]Department of Chemical Engineering, Pohang University of Science and Technology (POSTECH), Pohang, Gyeongbuk 37673, Republic of Korea. E-mail: jwhan@postech.ac.kr

[f]Institute of Engineering Research, Seoul National University, Seoul 08826, South Korea

[g]Advanced Institutes of Convergence Technology, Seoul National University, 145, Gwanggyo-ro, Yeongtong-gu, Suwon-si, Gyeonggi-do, 16229, Republic of Korea

† Electronic supplementary information (ESI) available. See DOI: https://doi.org/10.1039/d2ta08410d

‡ These authors contributed equally to this work.

reaction conditions, such as porous supports, high reaction temperatures, and H_2/N_2 or H_2/Ar atmosphere.[20–22] Therefore, the synthesis of SAAs in simple and mild conditions is still in imperative demand. Because cation exchange incorporates positively charged ions on the nanoparticle surface, it facilitates the synthesis of SAAs free from the aggregation of atoms through charge–charge interactions. The synthesized PdRu and PdCe catalysts exhibited similar mass activities and more than double high specific catalytic activities compared to commercial Pt/C catalysts in the methanol oxidation reaction (MOR) and hydrogen evolution reaction (HER), respectively, wherein Pt catalysts are mainly used.

Experimental

Synthesis of Pd nanocubes

For the synthesis of Pd nanocubes, 8 mL of an aqueous solution containing 36.93 mg of polyvinylpyrrolidone (PVP, MW = 55 000, Aldrich), 50 mg of L-ascorbic acid (AA, Aldrich), and 300 mg of potassium bromide (KBr, Aldrich) in a 20 mL vial was preheated to 80 °C with stirring at 800 rpm (stirred with a Teflon-coated magnetic stirring bar). Then, 3 mL of an aqueous sodium tetrachloropalladate (Na_2PdCl_4, 57 mg, Aldrich) solution was added to the vial using a pipette. The reaction solution was heated at 80 °C in air for 3 h. The product was collected by centrifugation and washed with a mixture of acetone and water. The synthesized Pd nanocubes were then re-dispersed in 11 mL of deionized (D.I.) water.[23]

Synthesis of 7 nm-sized spherical Pd nanoparticles

The spherical Pd nanoparticles were prepared using ethylene glycol (EG, Aldrich) as a solvent. 8 mL of EG solution containing 36.93 mg of PVP and 50 mg of AA in a 20 mL vial was preheated to 110 °C with stirring at 800 rpm. Then, 3 mL of EG solution containing 57 mg of Na_2PdCl_4 was added using a pipette. The final solution mixture was heated at 110 °C and kept for 3 h. After the reaction, the product was collected by centrifugation (10 000 rpm, 5 min) and washed with a mixture of acetone and water solution 3 times. The prepared spherical Pd nanoparticles were re-dispersed in 11 mL of D.I. water.

Removing PVP from the surface of Pd nanocubes

The washed Pd nanocubes were dispersed in 3 mL of acetic acid solution (≥99%, Aldrich) and aged at 90 °C for 3 h with magnetic stirring (800 rpm). After the reaction, the product was centrifuged and washed with a mixture of acetone and water 3 times and then re-dispersed in 11 mL of D.I. water.

Stabilizer exchange of Pd nanocubes from PVP to PEI

Pd nanocubes dispersed in 11 mL of D.I. water were transferred to a 20 mL vial. After adding 150 mg of PEI (Aldrich), the reacting solution was stored at 30 °C for 3 h with stirring (800 rpm). The product was centrifuged and washed with a mixture of acetone and water 3 times. The PEI-nanocubes were then re-dispersed in 11 mL of D.I. water.

Ru cation exchange into Pd nanoparticles

30 μL of HCl (12 M) solution was added to 11 mL of an aqueous suspension containing Pd nanoparticles. After stirring at 30 °C for 20 min, 1 mL of an aqueous ruthenium(III) chloride ($RuCl_3$, Aldrich) solution (the concentrations of $RuCl_3$ were 0.40 mg mL^{-1} for $PdRu_1$, 8.03 mg mL^{-1} for $PdRu_{20}$, 16.06 mg mL^{-1} for $PdRu_{40}$, 24.10 mg mL^{-1} for $PdRu_{60}$, and 40.16 mg mL^{-1} for $PdRu_{100}$, respectively) was added to the Pd nanoparticle suspension, and the mixture solution was aged at the same 30 °C for 3 h under 800 rpm stirring. The number after the sample represents the initial additional atomic percentage of Ru/Pd. The product was separated from the solution using centrifugation and washed with a mixture of acetone and water 3 times. The synthesized PdRu nanoparticles were re-dispersed in 11 mL D.I. water. To investigate the role of acidity of the solution, the pH of the solution was varied from 6.70 to 1.10 (by adjusting the pH with HCl) while keeping other experimental conditions unchanged. To observe the effect of high temperature, control experiments were performed at the reaction temperature of 95 °C. In addition, to study the role of water in Ru cation exchange, an experiment using 11 mL of dimethyl sulfoxide (DMSO) solution containing the same amount of Pd nanocubes instead of D.I. water suspension of Pd nanocubes was also conducted.

Various metal cation (Fe, Mn, Ce, and Eu) exchange into the Pd nanocubes

For the preparation of other metal cation exchange into Pd nanocubes (metal cations were Fe, Mn, Ce, and Eu, respectively), 1 mL of an aqueous solution containing metal precursors (6.28 mg mL^{-1} of $FeCl_3$ for $PdFe_{20}$, 6.70 mg mL^{-1} of $Mn(CH_3CO_2)_2$ for $PdMn_{20}$, 14.43 mg mL^{-1} of $CeCl_3 \cdot 7H_2O$ for $PdCe_{20}$, and 12.74 mg mL^{-1} of Eu $(CH_3CO_2)_3 \cdot xH_2O$ for $PdEu_{20}$, respectively) was used instead of $RuCl_3$ solution. Other experimental conditions were the same as for PdRu nanoparticles (all metal precursors are from Aldrich).

Ru and Eu metal cation exchange into Au nanoparticles

36.93 mg of PVP and 50 mg of AA were added into 8 mL of D.I. water and the reacting solution was heated to 80 °C with magnetic stirring (800 rpm). 3 mL of an aqueous $HAuCl_4 \cdot 3H_2O$ (Aldrich) solution (0.048 M) was then added into the solution and the resulting solution was aged at the same temperature for 3 h. The prepared Au nanoparticles were centrifuged, washed with acetone 3 times, and re-dispersed in 11 mL of D.I. water. 1 mL of 20 mol% Ru ($RuCl_3$; 8.03 mg mL^{-1}) and 1 mL of Eu (Eu $(CH_3CO_2)_3 \cdot xH_2O$ (0.64, 12.74 and 25.48 mg mL^{-1} for 1, 20 and 40 mol%, respectively)) cation exchange into the Au nanoparticles was conducted under the same conditions as those for PdRu and PdEu except that the synthesis was performed in the presence of Au nanoparticles instead of Pd nanoparticles.

Synthesis of Pd@Ru core@shell nanoparticles

30 μL HCl (12 M) was mixed with 11 mL of an aqueous solution containing 17.8 mg of Pd nanocubes and 80 mg AA, and the reacting solution was heated to 95 °C with magnetic stirring

(800 rpm). 1 mL of an aqueous $RuCl_3$ solution (The concentrations of $RuCl_3$ were 0.40 mg mL^{-1} for Pd@Ru-1, 8.03 mg mL^{-1} for Pd@Ru-20, and 16.06 mg mL^{-1} for Pd@Ru-40, respectively.) was injected into the solution, and the final solution was heated at 95 °C for 1 h. After the reaction, the product was centrifuged and washed with a mixture solution of acetone and water 3 times.

Characterization

TEM images were captured using a JEM-2100F microscope operating at 200 kV (JEOL, Akishima, Tokyo, Japan). High-resolution S/TEM images were captured using a JEM-ARM200F microscope (JEOL, Akishima, Tokyo, Japan) installed at the National Center for Inter-University Research Facility (Seoul National University, Seoul, South Korea). The microscope is operated at 200 kV and equipped with a cold field-emission gun and an aberration corrector in the probe-forming lens. EDS was performed using an X-Max silicon drift detector (SDD) (Oxford Instrument, Abingdon, United Kingdom) with an active area of 100 mm^2 and a solid angle of 0.9 sr installed in the microscope. The X-ray signals are collected by more than at least 100 000 counts, ensuring the accuracy of the results,[24] and the raw elemental maps are filtered by Wiener filter with a 3 × 3 kernel using Aztec software (Oxford Instrument, Abingdon, United Kingdom). To avoid the artefacts originating from the overlapping Pd L_α emission and Ru L_α emission with similar energies, Ru K_α emission is used instead to construct the elemental maps and the line profiles. ICP analyses were performed using a direct reading echelle ICP spectrometer (Leeman, Hudson, NH, USA). XRD patterns were measured using a Rigaku D-MAX/A diffractometer at 35 kV and 35 mA (Rigaku, Akishima, Tokyo, Japan), the X-ray source came from Cu Kα radiation ($\lambda = 1.5418$ Å). XPS results were checked by K-Alpha (Thermo Electron) using a PHI 5000 VersaProbe (ULVAC PHI, Chigasaki, Kanagawa, Japan).

Calculation details

The Vienna ab initio Simulation Package (VASP) was used to perform spin-polarized density functional theory (DFT) calculations with the plane-wave approach.[25] For the exchange–correlation energy descriptions, the Perdew–Burke–Ernzerhof (PBE) functional of the generalized gradient approximation (GGA) was used.[26] The effect of core electrons on the valence electron density was represented using the projector augmented wave (PAW) method. For self-consistent iterations, the energy cutoff and convergence threshold were set to 400 eV and 2×10^{-4} eV, respectively, while geometry optimizations were considered to be converged when the residual forces were less than 0.03 eV $Å^{-1}$.

A 4 × 4 × 4 supercell was used for bulk $Pd_{32-x}Ru_x$ alloy calculation. Pd (100) and Au(100) slabs were modeled using a (3 × 3) surface unit cell with eight layers of thickness to describe the exchange of $RuCl_3$ and Pd atoms in Pd nanocubes, while other calculations were performed using four-layer slab models. We confirmed that the differences in $RuCl_3$ adsorption energy and first exchange reaction enthalpy are negligibly small (less than 0.05 eV) between the four-layer slab model and eight-layer slab. The calculations for the cation exchange of large Mn precursors ($Mn(CH_3CO_2)_2$) were performed using a (4 × 4) surface unit cell of Pd (100) to avoid lateral interactions. Half of the layers of the slab models were fixed, whereas the positions of all other atoms were fully relaxed. To avoid interactions between virtual periodic slabs, the slabs were separated by a vacuum layer greater than 10 Å. The gas-phase molecules were calculated in a cubic unit cell of 15 Å. The Brillouin zones were sampled using Monkhorst–Pack (MP) *k*-point sampling for all bulk and slab models, while all gas molecules were calculated using Γ–centered 1 × 1 × 1 grid.[27] 4 × 4 × 4, 4 × 4 × 1, and 3 × 3 × 1 MP *k*-point samplings were used for the geometric optimization of $Pd_{32-x}Ru_x$ bulk alloy, (3 × 3) Pd (100) surface, and (4 × 4) Pd (100) surface, respectively.

The transition state (TS) configurations and minimum energy pathways (MEPs) were optimized using the climbing image nudged elastic band (CI-NEB) method.[28] Here, 3–5 intermediate images were used to determine the MEPs until the maximum atomic forces converged less than 0.03 eV $Å^{-1}$. The charge transfers between the surface and the adsorbates were estimated by employing the Bader charge analysis.[29] Alloy formation energy was represented by the bulk energy difference between alloyed metal and pure metal as follows:

$$E_{\text{alloy form}} = E(Pd_{32-x}Ru_x) - (32 - x)\,E(Pd) - xE(Ru),$$

where $E(Pd_{32-x}Ru_x)$ represents the total energy of $Pd_{32-x}Ru_x$ bulk alloy ($x = 0$–4), while E(Pd) and E(Ru) are the bulk energy per atom.

To simulate X-ray diffraction (XRD) patterns of the four PdRu with different Ru^{3+} concentrations, 8 × 8 × 8 supercells composed of 256 atoms were constructed; Pd_{256}, Ru_1Pd_{255} (Ru 0.39%), Ru_2Pd_{254} (Ru 0.79%), and Ru_3Pd_{253} (Ru 1.19%), and 1 × 1 × 1 MP *k*-point samplings were used for the geometric optimization. The Ru concentrations of the four bulk models were chosen based on the ICP analysis of the synthesized PdRu samples (Table S1†). Three electrons per Ru cation were deducted from the supercell to simulate the cation exchanged system. We confirmed that the positive charges are mostly localized around Ru atom (+0.21–+0.26 per Ru atom), and extra positive charges on Pd are negligibly small (less than +0.03 per Pd atom). The details for relative energy diagram calculations of the PdRu exchange reaction (Fig. 3b) can be found in the ESI Note.† The reaction free energy of MOR and HER were calculated using the computational hydrogen electrode model proposed by Nørskov *et al.* as follows:[30]

$$\Delta G = \Delta E + \Delta ZPE - T\Delta S - neU,$$

where ΔE denotes the reaction energy obtained from the DFT calculations, ΔZPE is the DFT-calculated zero-point energy, S is the standard entropy taken from NIST Chemistry WebBook, the coefficient n refers to the number of transferred electrons, U is the applied potential in RHE scale, and T is set to 298.15 K. The adsorption energy (E_{ads}) was defined as follows:

$$E_{ads} = E_{mol/slab} - E_{slab} - E_{mol},$$

where $E_{mol/slab}$ is the total energy of the molecule-adsorbed slab system, E_{slab} is the total energy of the pristine slab, and E_{mol} is the total energy of the DFT-calculated gas-phase molecule.

Electrocatalysis test

In order to immobilize the catalyst onto carbon particles with precisely ratio and amounts, we checked the concentration of Pd, $PdRu_{(1,20,40)}$, Pd@Ru_{20} core–shell, Pd + HCl, Pd + $RuCl_3$, $PdCe_{20}$, and $PdEu_{20}$ nanoparticle suspensions by ICP measurement. Then, 3 mg of catalyst was mixed with 20 mL of ethanol solution containing 15 mg of Vulcan XC-72 carbon (purchased from CABOT (St. Louis, MO, USA)). The ethanol/water mixture solution containing the catalyst and carbon was heated at 73 °C under magnetic stirring (800 rpm). After 1 h aging, carbon-supported nanoparticles were collected by centrifugation and re-dispersed in ethanol. The concentration of metal in the final solution was fitted to 3 mg mL^{-1} for the electrocatalysis test.

Before the electrochemical tests, we prepared Nafion-based ink slurry. 600 μL of ethanol ink slurry was composed of 333 μL of carbon-supported nanoparticle dispersion (the concentration of metal was 3 mg mL^{-1}), 45 μL of Nafion solution (~5 wt% in a mixture of lower aliphatic alcohols and water, Aldrich), and 222 μL of ethanol. The metal concentration of the final solution was 1.67 mg mL^{-1}. Electrochemical measurements were performed using a standard three-electrode cell connected to a CHI 760E potentiostat (CH Instruments, Austin, TX, USA) at room temperature. The three-electrode system consists of a Pt mesh (1 × 1 cm^{-2}) or graphite rod as the counter electrode, a leak-free AgCl/Ag/KCl electrode as a reference electrode, and a glassy carbon (GC) rotating disk electrode (RDE, 5 mm diameter, Pine Research Instrumentation, Durham, NC, USA) as the working electrode, respectively. To prepare the working electrode, 4.7 μL ethanol ink slurry was transferred onto the glassy carbon RDE with a geometric area of 0.196 cm^2. The loading amount for all catalysts was 7.84 μg. After evaporation of ethanol, the cyclic voltammetry (CV) measurements were carried out under a flow of N_2 (airgas, ultrahigh purity) at a sweep rate of 50 mV s^{-1} in 1 M potassium hydroxide (KOH) for the methanol oxidation reaction (MOR). The electrochemical surface areas (ECSA) were estimated by the reduction region of PdO to Pd between −0.9 and 0.1 V. For Pd oxide reduction, the oxide reduction peak of PdO at around −0.23 V *vs.* Ag/AgCl[31] in 1 M KOH was used to calculate the ECSA by eqn (1).[32]

$$ECSA_{PdO}\ (m^2\ g^{-1})\ \left[\frac{Q_{PdO}(C)}{S(uC\ cm^{-2})\cdot l\ (mg)}\right] \times 10^5 \qquad (1)$$

where Q is the charge measured in coulombs (C), S is the conversion factor that is equal to the reduction monolayer charge multiplied by the electrode surface area ($S = Q^{O}_{red,ML,S} \times 0.196\ cm^{-2}$), the reduction monolayer charge ($Q^{O}_{red,ML,S}$) of Pd and Pt oxide is 420 μC cm^{-2},[32,33] and l is the amount of catalyst loaded ($l = 0.00784$ mg). The electrochemical measurements for the methanol oxidation reaction (MOR) were performed at room temperature in a solution containing 1 M KOH and 1 M methanol under a flow of N_2. CV curves were collected at a sweep rate of 50 mV s^{-1} and a scan range of −0.9 V ~0.1 V. The hydrogen evolution reaction (HER) was performed using the same three-electrode system but using a graphite rod as the counter electrode, the same ink slurry making process as MOR, and the loading amount was also 7.84 μg. The initial HER activity test was conducted by linear sweep voltammetry (LSV) from 0 to −0.30 *vs.* reversible hydrogen electrode (RHE) with a scan rate of 5 mV s^{-1} in 0.5 M sulfuric acid (H_2SO_4). The Ag/AgCl was used as a reference electrode, and the potential was transferred RHE. CV measurements were scanned from 0.05–1.05 V *vs.* RHE at a sweep rate of 5 mV s^{-1} in 0.5 M H_2SO_4 solution. The ECSA of HER was determined by the Pd–O reduction also. The Pd and Pt oxide reduction peak located at about 0.75 V was used for ECSA calculation[33,34] using eqn (1).

The reference electrode (Ag/AgCl) chamber was filled with a saturated KCI solution with the Cl^- concertation of 3 mol L^{-1}. The measured potentials *vs.* Ag/AgCl were converted to the reversible hydrogen electrode (RHE) scale according to the Nernst equation:[35]

$$E_{RHE}\ (V) = E_{Ag/AgCl} + E^{o}_{Ag/AgCl} + 0.059 \times pH \qquad (2)$$

where $E^{o}_{Ag/AgCl} = 0.1976$ V at 25 °C, $E_{Ag/AgCl}$ is the experimentally measured potential *versus* the Ag/AgCl (KCl sat.) reference electrode, and pH denotes the pH of the electrolyte. Here, the pH is 13.6 and 0 when the electrolyte is 1 M potassium hydroxide (KOH) and 0.5 M sulfuric acid (H_2SO_4), respectively. Thus, $E_{RHE}\ (V) = E_{Ag/AgCl} + 1$ when the electrolyte is 1 M potassium hydroxide (KOH), and $E_{RHE}\ (V) = E_{Ag/AgCl} + 0.1976$ when the electrolyte is 0.5 M sulfuric acid (H_2SO_4).

Results and discussion

As a base material for cation exchange, Pd nanocubes with an average side dimension of 13 nm were prepared using a previously reported method (Fig. S1†).[23] Ru cations were exchanged for Pd atoms by adding an aqueous $RuCl_3$ solution to a Pd nanocube suspension under acidic conditions (pH 1.39) at 30 °C. Fig. S2† shows transmission electron microscopy (TEM) images of Pd nanocubes treated with 1, 20, 40, 60, and 100 mol% of $RuCl_3$ compared to Pd (hereinafter referred to as $PdRu_1$, $PdRu_{20}$, $PdRu_{40}$, $PdRu_{60}$, and $PdRu_{100}$, respectively). The nanoparticle size and morphology were approximately the same as those of the original Pd nanocubes. Although the Ru content in the PdRu slightly increased with increasing $RuCl_3$ concentration, the Ru content in Pd did not proportionally increase with increasing $RuCl_3$ concentration. Even when the $RuCl_3$ concentration increased to 40, 60, and 100 mol%, the Ru content in the PdRu did not exceed the maximum of 1.42 mol% (Table S1†). The high-resolution TEM (HRTEM) image of the $PdRu_{20}$ shows that the Pd nanocube surfaces were smooth and bump-free, indicating the absence of small Ru clusters on the surface (Fig. 1a). Fig. 1b–d, S3 and Fig. S4† show energy-dispersive X-ray spectroscopy (EDS) results of $PdRu_{20}$,

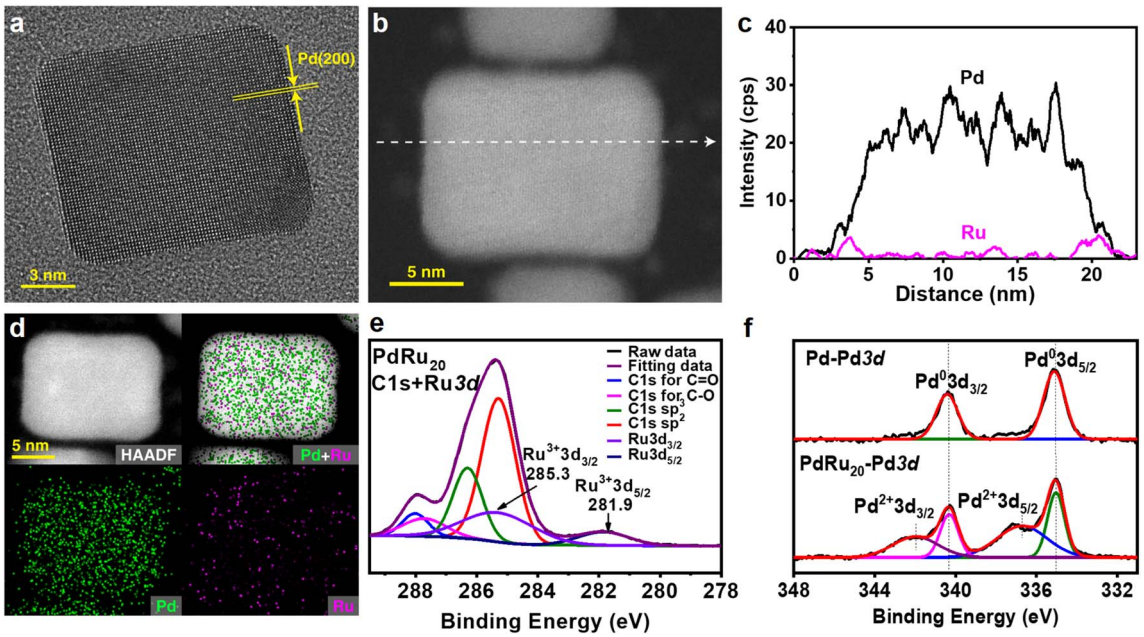

Fig. 1 Characterization of $PdRu_{20}$. (a) HRTEM image and (b) high-angle annular dark-field (HAADF) STEM image of $PdRu_{20}$. (c) EDS line profile for Pd and Ru along the line shown in (b). (d) HAADF-STEM images and EDS elemental maps of $PdRu_{20}$. (e) Ru 3d with C 1s and (f) Pd 3d XPS spectra of Pd and $PdRu_{20}$.

revealing that Ru cations are distributed over the entire nanoparticle while many of them are concentrated near the nanoparticle surface due to the relatively high activation barrier for the diffusion. Fig. 1e shows the X-ray photoelectron spectroscopy (XPS) peaks of the $PdRu_{20}$, which could be deconvoluted into 8 peaks containing XPS C1s and Ru3d peaks. The binding energies of Ru were 281.9 eV for $Ru3d_{5/2}$ and 285.3 eV for $Ru3d_{3/2}$, respectively, which could be assigned to Ru^{3+} rather than Ru^0.[36,37] The $Pd3d_{3/2}$ and $Pd3d_{5/2}$ XPS peaks of $PdRu_{20}$ at binding energies of 335.1 and 340.3 eV were consistent with XPS peaks of the Pd nanocubes (Fig. 1f). Significantly, the peaks at 336.7 eV and 342.1 eV in the $PdRu_{20}$ correspond to Pd^{2+}. [38] It indicated that a small amount of Pd^{2+} was formed after the cation exchange reaction.

Based on the XPS result, we simulated X-ray diffraction (XRD) patterns of PdRu (Fig. 2a). Due to the low Ru^{3+} concentration, the crystal structure of PdRu was more like that of Pd than that of Ru. The simulated XRD peaks of PdRu were shifted to a higher angle by increasing the amount of Ru^{3+}, indicating the host crystalline lattice of Pd shrunk due to the small radius of Ru^{3+} (68 pm) compared with that of Pd (140 pm). Measured XRD patterns of PdRu were shifted to a high angle by increasing the Ru content, showing that it was consistent with the calculation results (Fig. 2b). To investigate the difference of XRD patterns between Ru^{3+} doped Pd and Pd core@Ru species shell structure, Pd@Ru core@shell nanoparticles containing 3∼12 mol% of Ru were prepared by reducing a Ru precursor with a reducing agent (Fig. S5, Table S2,† hereinafter referred to as $Pd@Ru_1$, $Pd@Ru_{20}$, and $Pd@Ru_{40}$, respectively). HRTEM images of $Pd@Ru_{20}$ show the presence of bumps on the surface, indicating the formation of Ru species on the surface of Pd nanocubes (Fig. 2c). The Ru3d XPS peaks at 284.7 and 281.5 eV of $Pd@Ru_{20}$ were well matched with XPS peaks of RuO_2 while oxidation state of Pd remained 0, indicating that the synthesized core@shell nanoparticles were Pd core@RuO_2 shell structure (Fig. S6a and b†).[39] As we expected, XRD patterns of Pd@Ru demonstrated the low angle shifting due to the lattice expansion of Pd by attaching RuO_2 on the surface (Fig. 2d). This result indicates that Ru cations, not in oxide form, are distributed inside PdRu.

The process of Ru cation exchange was further investigated at the atomic level using density functional theory (DFT) calculations. The overall cation exchange process can be simplified into four steps: (1) charge transfer from PVP to Pd nanocubes, (2) $RuCl_3$ adsorption onto the Pd nanocubes, (3) exothermic exchange of $RuCl_3$ with a lattice Pd atom in Pd nanocubes, (4) dissolution of chlorinated Pd in the presence of HCl (Fig. 3a). Relative reaction enthalpy for exchanging $RuCl_3$ with a surface Pd atom was obtained using gaseous $RuCl_3 \cdot (H_2O)_3$ as a reference state (Fig. 3b). Starting from the exothermic adsorption of $RuCl_3$ onto Pd (100) surface (−0.79 eV), a kinetic barrier of 0.58 eV is required to dissociate Ru–Cl bonds and to pull out one Pd atom from the Pd surface. The first exchange between the Ru cation and the outermost Pd atom occurs exothermically (−1.57 eV), leaving one chlorinated Pd atom on the surface. This exothermic exchange of the Ru cation can be understood by the surface instability caused by the addition of Ru cation on the Pd surface, as Ru has higher surface energy than Pd. From the enthalpy change of the Ru cation exchange with a deeper Pd layer, it is shown that the exchange reaction becomes less favorable than the first exchange because the Ru atom in bulk Pd is unstable, as

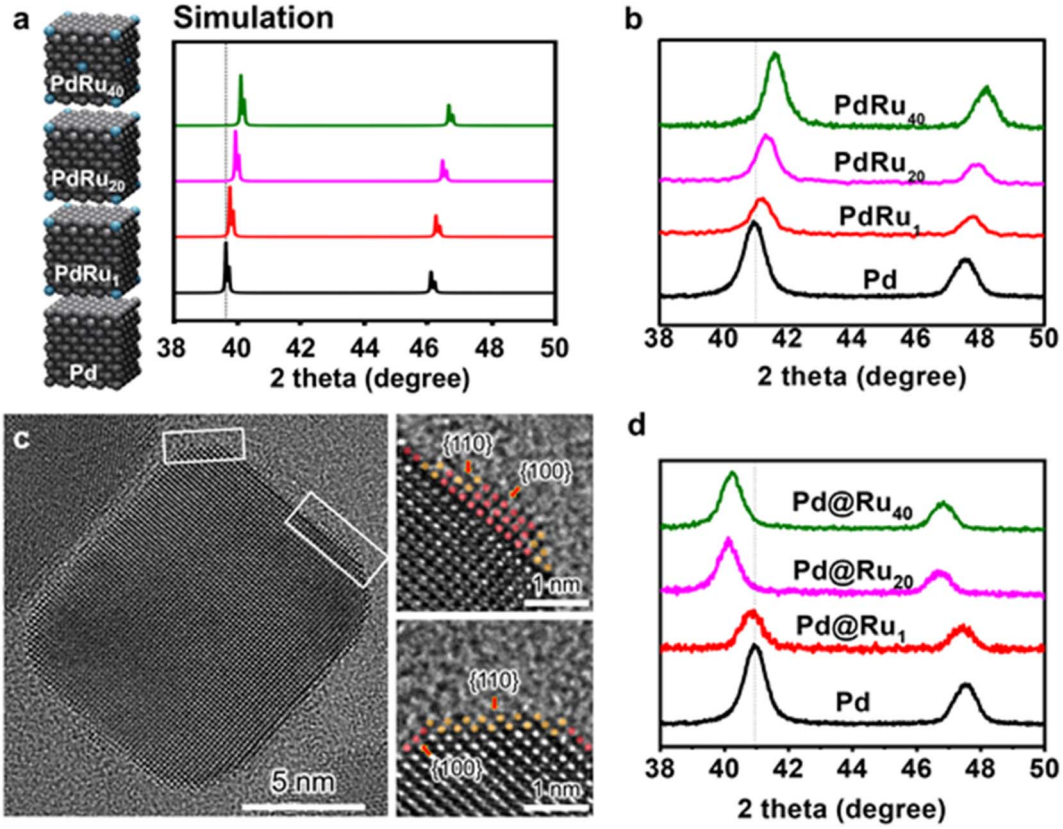

Fig. 2 Characterization of PdRu and Pd@Ru. (a) Simulated and (b) measured XRD patterns of Pd and PdRu. (c) HRTEM images of Pd@Ru_{20}. (d) XRD pattern of Pd@Ru core@shell nanoparticles.

indicated by the unfavorable bulk alloy formation energy between Ru and Pd (Fig. S7†). Furthermore, the exchange reactions in deeper Pd layers also require higher kinetic barriers than the first exchange (0.58 eV), since the Ru atom is fully coordinated by Pd atoms, resulting in less space for the Ru atom to exchange with the Pd atom in the deeper layer. Therefore, most of the Ru cations spontaneously exchange only with a few layers of Pd, as clearly seen in the EDS elemental maps and line scans, which show that most of the Ru cations stay near the surface of Pd nanocube (Fig. 1c). Similar exothermic enthalpy change for the exchange were observed for the first exchange reaction of Ce, Fe, and Mn cations with Pd (100) (Fig. S8†).

The Pd nanocubes used in the present reaction are coated with an organic stabilizer, polyvinylpyrrolidone (PVP). To understand the role of PVP in Ru cation exchange, we prepared PVP-free Pd nanocubes by washing the Pd nanocubes after acetic acid treatment and using them for Ru cation exchange. Thermogravimetric analysis-differential scanning calorimetry (TGA-DSC) and Fourier-transform infrared (FT-IR) spectroscopy show that most of the PVP had been removed from the Pd nanocube surface, while the nanocubes maintained their original size and morphology (Fig. S9 and S10†). The TEM images of $PdRu_{20}$ prepared using the PVP-free Pd show the formation of round-cornered nanocubes after the Ru cation exchange (Fig. S11†). The XRD patterns of the product show that none of the peaks are shifted to a higher angle, indicating that Ru cations did not penetrate the PVP-free Pd nanocubes (Fig. S12†). According to the Bader charge analysis, *N*-vinylpyrrolidone, the monomer of PVP, donates excess electrons to the Pd nanocubes (Fig. 3c), which in turn promotes Ru cation exchange by drawing more $RuCl_3$ to the nanocube surface (Fig. 3d). In fact, because the PVP-free Pd exhibits a zeta potential of −6.43 mV (at pH 1.39), it was less negatively charged than the PVP-coated Pd (−13.8 mV at pH 1.39, Table S3†). To determine how the charges in the stabilizer affect the cation exchange reaction, the PVP was replaced with positively charged polyethyleneimine (PEI) (Fig. S13†). Owing to its amine functional groups, the PEI-stabilized Pd nanocubes were positively charged with a zeta potential of 32.33 mV at pH 1.39, (Table S4†), and the XRD peaks did not shift after the addition of $RuCl_3$ (Fig. S14†). Additionally, the morphologies of the PEI-stabilized Pd and PEI-$PdRu_{20}$ both remained unchanged (Fig. S15 and S16†), suggesting that the charge–charge interaction between the Ru cations and the negatively charged surfaces of the PVP-stabilized Pd nanocubes were a driving force for the Ru cations to access the Pd nanocubes.

The present experiment was carried out in an acidic aqueous solution (pH 1.39), and we found that the XRD peaks did not shift when the reaction was performed under neutral conditions (pH 6.7, Fig. S17†). To reveal the role of acidic conditions in Ru cation exchange, we performed further DFT calculations and characterization (Fig. S18†). Because Ru cation exchange

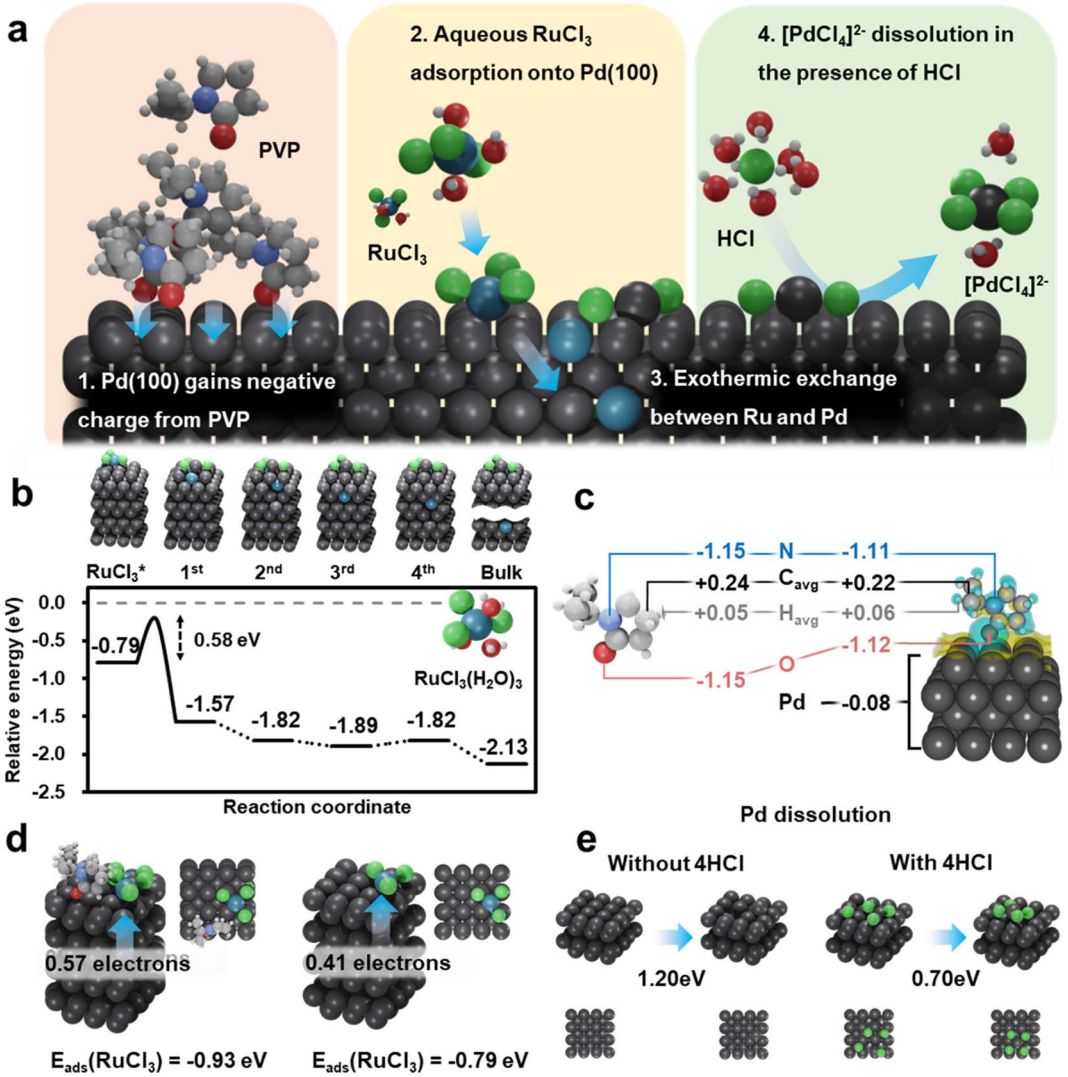

Fig. 3 Mechanism studies of exchange of Ru^{3+} and Pd. (a) Schematic illustration of the spontaneous cation exchange mechanism between $RuCl_3$ and Pd nanocubes in four steps: (1) excess charge accumulation on Pd nanocubes, (2) $RuCl_3$ adsorption onto Pd nanocubes, (3) exothermic exchange between $RuCl_3$ and a lattice Pd atom in Pd nanocubes, and (4) dissolution of chlorinated Pd. (b) Relative energy diagram of $RuCl_3$ exchange on Pd (100) surface. The dashed gray line denotes the reference energy of $RuCl_3{\cdot}(H_2O)_3$. (c) Bader charge analysis of a gas-phase *N*-vinylpyrrolidone molecule and *N*-vinylpyrrolidone adsorbed on the Pd (100) surface. (d) Number of transferred electrons from Pd to $RuCl_3$ and $RuCl_3$ adsorption energy with and without *N*-vinylpyrrolidone. (e) Reaction energy of Pd dissolution on the Pd (100) without HCl (left) and with four pre-adsorbed HCl (right). (Color code: Pd: dark gray, Ru: blue, N: light blue, Cl: green, C: gray, H: white, and O: red).

initially requires a Pd atom to be removed from the Pd surface, thermodynamically favorable Pd dissolution should promote Ru cation exchange. Compared to the high Pd dissolution energy (1.20 eV) on the pristine Pd surface, the Pd dissolution energy is significantly reduced to 0.70 eV when four additional HCl molecules are adsorbed on the Pd surface to form tetrachloropalladium(II), $[PdCl_4]^{2-}$, which was identified as the dominant chlorinated Pd complex formed under acidic conditions (Fig. 3e).[40,41] When Pd is dissolved in the solution, leaving a vacancy on the surface, the strength of $RuCl_3$ adsorption increased considerably at the Pd surface vacancy (−1.17 eV) compared to the pristine Pd surface (−0.79 eV). The adsorbed $RuCl_3$ then occupies the Pd vacancy, exhibiting an additional exothermicity of −1.46 eV while dissociating the Ru–Cl bonds (Fig. S19†). Inductively coupled plasma mass spectrometry (ICP–MS) measurements corroborated the hypothesis that the amount of Pd in the solution increased after the exchange reaction (0.576%) compared with only the HCl treatment (0.150%, Table S5†). The UV-vis spectrum of the supernatant of Pd shows the presence of two distinctive absorbance peaks at 224.14 and 239.49 nm, which correspond to $[PdCl_4]^{2-}$ (Fig. S20†).[42] The ICP-MS measurements and UV-vis spectra confirm that Pd is easily dissolved in an acidic solution and the presence of $RuCl_3$ to form $[PdCl_4]^{2-}$, thereby supporting the theoretical predictions. With decreasing pH, the XRD peak shifted from 41.37° (at pH 1.91) to a higher angle of 41.82° (at pH 1.10) compared to the XRD peak of the pure Pd. (Fig. S17†). In addition, the XRD peak did not shift without the addition of

Ru cations, suggesting that the Ru cations were responsible for the XRD shift (Fig. S21†). When the Ru cations were exchanged at a high temperature of 95 °C, we also observed the XRD peak shifting (Fig. S22†), and the original $PdRu_{20}$ morphology was maintained (Fig. S23†). The XRD peak shifting was also observed when dimethyl sulfoxide (DMSO) was used as the solvent instead of water, confirming that the reaction was independent of the solvent (Fig. S24†). The Pd nanocubes were bound by {100} facets to control the analysis uncertainty. DFT calculations for Ru cation exchange on the basal plane ({111} facets) and edge ({211} facets) also show an exothermic trend similar to that for Ru cation exchange on the cubic plane ({100} facets), thereby further supporting the morphology independence (Fig. S25†). We found the XRD peak shifting to a higher angle with 7 nm-sized spherical Pd nanoparticles surrounded by various facets instead of the Pd nanocubes, confirming that the Ru cation exchange was independent of the Pd nanoparticle morphology (Fig. S26–S28†).

We conducted comparative experiments to determine whether this cation exchange reaction we found was expandable to systems with various cations and metal nanoparticles. When cerium (Ce), europium (Eu), iron (Fe), and manganese (Mn) cations were used instead of Ru cations for the exchange reaction, the XRD peaks of prepared $PdCe_{20}$, $PdEu_{20}$, $PdFe_{20}$, and $PdMn_{20}$ were shifted to higher angles compared to the pure Pd while keeping their size and morphology unchanged, indicating that these metal cations could be readily exchanged with Pd (Fig. 4a–c, S29–S31 and Table S6†). Fig. 4a and b show that a small amount of Ce cations was in the Pd, indicating the formation of Ce cation-doped Pd nanocubes. DFT calculations of the Ce cation exchange reaction showed that only the first exchange step is exothermic, while exchange steps with deeper Pd layers are endothermic due to the large size of the Ce cation (Fig. S32†). This is well consistent with the EDS mapping result where the Ce cations stay at the outmost surface of Pd nanocubes (Fig. 4b). When Au nanoparticles were used instead of Pd nanocubes, Ru cation-doped Au nanoparticles were formed ($AuRu_{20}$, Fig. 4d–f, S33, and S34†). According to the DFT results of the Ru cation exchange reaction with Au (100), the reaction is slightly endothermic for the first and second exchange reaction steps but becomes exothermic as the Ru proceeds deeper into the Au bulk region (Fig.S35†). The EDS mapping clearly shows that the Ru atoms were well distributed throughout the Au nanocubes, which is consistent with the theoretical predictions (Fig. 4e). Furthermore, Eu cations were also exchanged with Au nanoparticles, thereby confirming that various metal cations and nanoparticles are exchangeable in the cation exchange reaction (Fig. S36–S38 and Table S7†).

Owing to charge–charge repulsion, the exchanged cations are well dispersed over the surface of a metal nanoparticle without aggregation. Therefore, the synthesized metal alloy nanoparticles can act as good SAAs. We measured the catalytic activity of PdRu in the MOR, an electrochemical reaction in which Pt exhibits the best catalytic activity. The Pd and PdRu were dispersed on carbon particle surfaces to obtain a large electrochemical surface area (ECSA) (Fig. S39†). The $PdRu_1$/C containing 0.33 mol% Ru cations exhibited 2.5 times higher mass activity than Pd/C (557 mA mg^{-1}), and similar mass

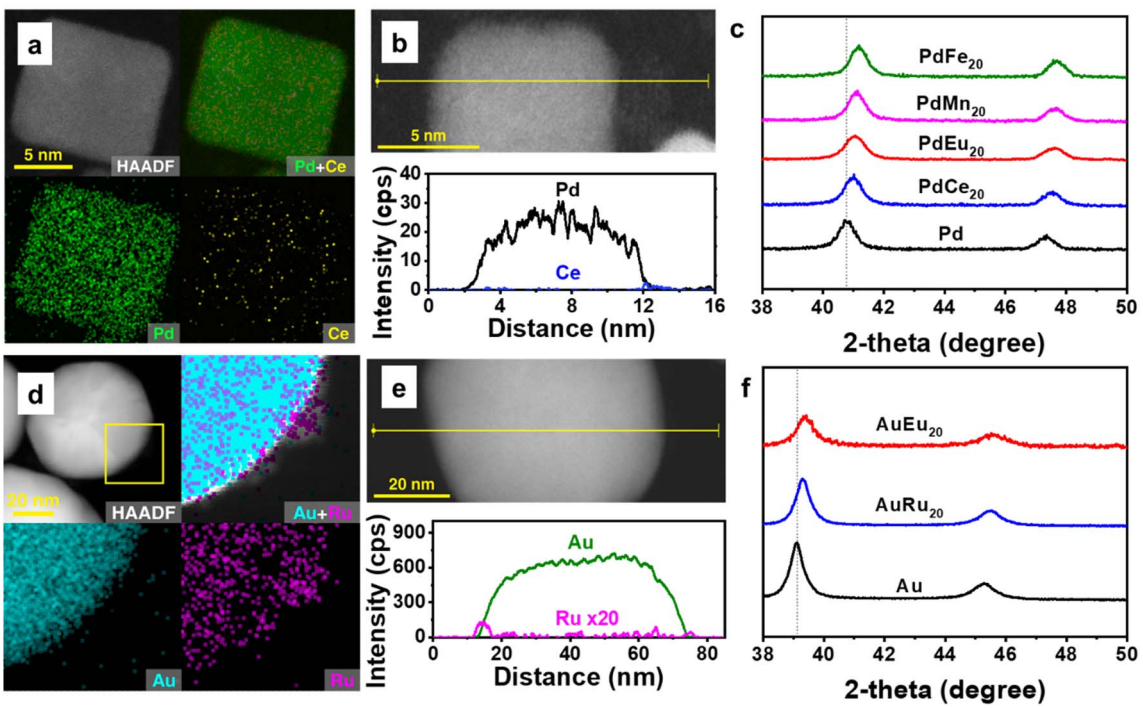

Fig. 4 PdM (M = Ce, Eu, Mn, Fe) and AuM (M = Ru and Eu) nanoparticles by using spontaneous cation exchange. (a) EDS mapping of $PdCe_{20}$, (b) HAADF-STEM image and EDS line profile for Pd and Ce, along the line marked in the HAADF-STEM image, (c) XRD patterns of PdM (M = Ce, Eu, Mn, and Fe), (d) EDS mapping of $AuRu_{20}$, (e) HAADF-STEM image and EDS line profile for Au and Ru, along the line marked in the HAADF-STEM image. The intensity of Ru is multiplied by 20, (f) XRD patterns of AuM (M = Eu and Ru).

activity compared with the commercial Pt/C (1354 mA mg^{-1}) (Fig. 5a and b). The $PdRu_1$/C catalyst had a smaller ECSA (26.35 m^2 g^{-1}) than the commercial Pt/C catalyst (56.54 m^2 g^{-1}) because of the larger size of the $PdRu_1$ (13 nm) than the size of Pt nanoparticles in the commercial Pt/C (2.2 nm) (Fig. S39, S40 and Table S9†). In other words, the $PdRu_1$/C displayed 2.5 times higher specific catalytic activity than the Pt/C (Fig. 5a). Interestingly, the electrochemical reactivity of PdRu/C gradually decreased with increasing Ru content (Fig. 5a and b). It should be noted that the CV curves exhibited two characteristic anodic peaks for all the samples, one in the anodic curve and the other in the cathodic curve (Fig. 5b). These abnormal anodic peaks in the cathodic curves are attributable to the residual carbonaceous species, indicating the presence of residual intermediates on the catalyst surface after MOR. The peak will appear when these carbonaceous intermediates are desorbed from the catalyst at low potential.[43,44]

To elucidate the mechanism of enhanced catalytic activities of PdRu and characteristic anodic peaks in CV curves, a free diagram of all the possible MOR pathways on the bare Pd and PdRu models was generated using DFT calculations (Fig. 5c and Table S8†). The minimum potential barrier required for the MOR pathway from methanol to carbon dioxide was determined (Fig. 5c). Because Ru is oxophilic, the binding of methanol (CH_3OH) on the PdRu surface is considerably promoted compared to that on the bare Pd surface.[45] Furthermore, the first dehydrogenation step (from CH_3OH to CH_2OH), which was the potential determining step (PDS) of the MOR for both surfaces, could be facilitated in the presence of Ru cations. The overall potential requirement in the PdRu is much lower than the one in pristine Pd because oxygen-containing MOR intermediates strongly interact with the oxophilic Ru on the surface. Therefore, the enhanced MOR activity of PdRu is attributed to the optimized interaction of MOR intermediates with the PdRu surface. Furthermore, CO* formed during the MOR could be bound strongly on both Pd and PdRu surfaces, with adsorption free energies of −0.74 eV and −1.01 eV, respectively (Table S8†). We found that $*CH_2O$ and $*CH_3OH$ are also stably bound on the PdRu surfaces with negative adsorption free energy (−0.66 eV and −0.42 eV, respectively). Therefore, the abnormal anodic peak in the cathodic curves can be understood as the removal of the residual MOR intermediates, including *CO and $*CH_2O$, during the cathodic sweep at low potential.

For comparison, the mass and specific activities of the $Pd@Ru_{20}$ core–shell nanoparticles were both lower than the PdRu counterparts (Fig. 5a, b, S41, S42, and Table S9†). In addition, MOR activities of Pd nanocubes treated with HCl (pH of 1.39) and the PdRu prepared under neutral conditions (pH of 6.7) show no dramatic enhancement (Fig. S43†). These results indicated that well-dispersed Ru cation on the Pd surface would increase the MOR activity.

We also introduced $PdCe_{20}$ and $PdEu_{20}$ to HER as electrocatalysts, in which Pt has conventionally been used as the main catalyst. The $PdCe_{20}$/C exhibited 82% geometrical activity (compared to commercial Pt/C) at the current density of 10 $mAcm^{-2}$ and 1.5 times higher specific activity at the potential of 70 mV (Fig. 6a, b, S44, S45, and Table S10†). Fig. 6c is the corresponding Tafel plots constructed from the LSV voltammograms in the range of 0–10 mA cm^{-2}. $PdCe_{20}$ displayed a Tafel slope of 38 mV dec^{-1}, which was obviously lower than 92 mV dec^{-1} for pure undoped Pd, indicating much better HER kinetics and catalytic activity after Ce cation doping. The experimentally determined HER activity is compared with the hydrogen adsorption free energy (ΔG_H) obtained from DFT calculations. The ΔG_H of rare-earth metal cation-alloyed Pd follows a volcano relationship for both the overpotential and exchange current

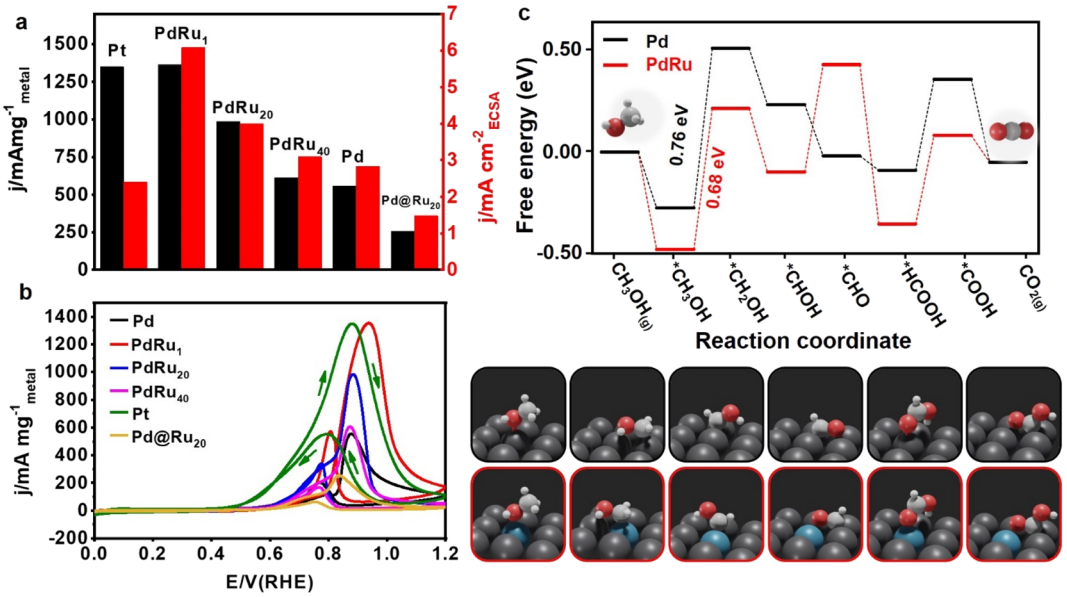

Fig. 5 MOR electrocatalytic activities of PdRu. (a) Mass and specific activities and (b) CV curves of Pd/C PdRu/C, $Pd@Ru_{20}$/C, and the commercial Pt/C catalyst (E-TEK) towards MOR recorded at room temperature in an N_2-purged 1 M potassium hydroxide (KOH) and 1 M methanol solution with a sweep rate of 50 mV s^{-1}. (c) Free energy diagram of MOR to CO_2 on Pd(100) and PdRu (100). (Color code: Pd: dark gray, Ru: blue, C: gray, H: white, and O: red).

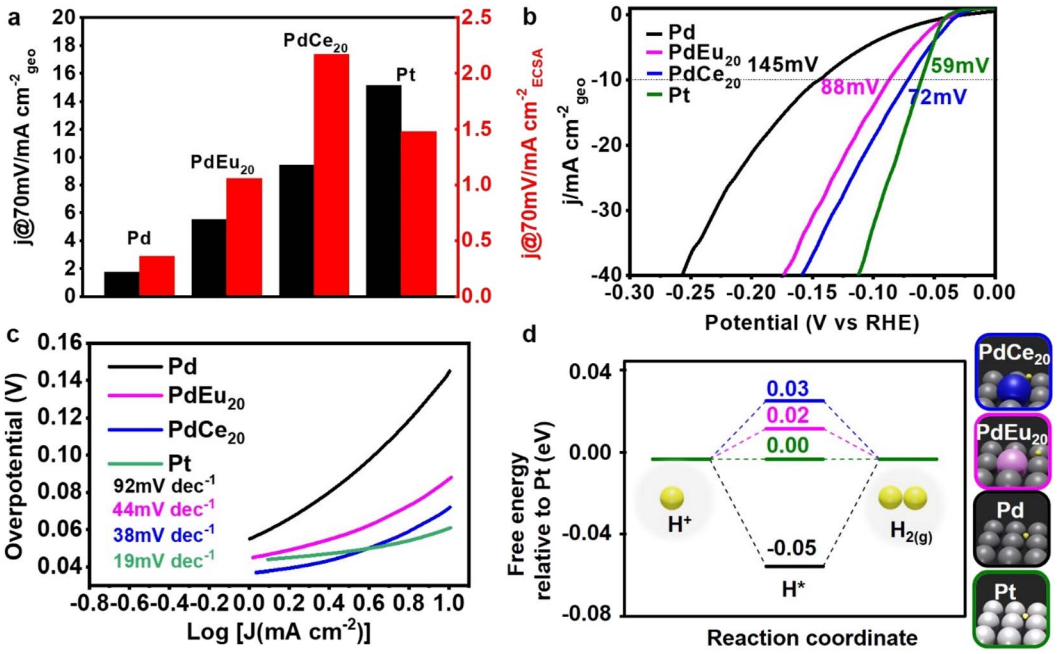

Fig. 6 HER electrocatalytic activities of PdCe and PdEu. (a) The geometrical and specific activities in HER and LSV curves of Pd, $PdEu_{20}$, $PdCe_{20}$, and commercial Pt normalized by geometric surface area and by estimated ECSA (at −70 mV *versus* RHE) histogram in N_2 saturated 0.5 M H_2SO_4 solution with a scan rate of 5 mV s^{-1} (b) LSVs recorded figure of Pd, $PdEu_{20}$, $PdCe_{20}$, and commercial Pt. (c) Tafel plots of Pd, $PdEu_{20}$, $PdCe_{20}$, and commercial Pt in 0.5 M H_2SO_4 at 5 mV s^{-1}. (d) Free energy diagram of HER on Pd(100), PdEu(100), PdCe(100), and Pt(100). (Color code: Pd: dark gray, Ce: blue, Eu: pink, H: yellow, and Pt: white gray).

density.[46] The $PdCe_{20}$ surface exhibits approximately the same ΔG_H as Pt (111), thereby positioning a narrow range at the summit of the HER activity volcano. The DFT results implied that the cation-exchange-induced enhanced HER activities could be attributed to the optimized interaction between the catalyst surface and reaction intermediates, which is closely correlated with the doped cations (Fig. 6d).

Conclusions

We have reported the discovery of a novel cation exchange phenomenon between the metal cation and metal nanoparticles at the nanoscale and utilizing it for the preparation of highly efficient SAAs. SAAs were easily synthesized by adding transition cations, including Ru^{3+}, Ce^{3+}, Eu^{3+}, Fe^{3+}, and Mn^{2+}, into Pd or Au nanoparticles suspension. Through DFT calculations and comparative experiments, we found that this exchange occurs spontaneously by charge–charge interaction between the positively charged metal cation and negatively charged metal nanoparticles. The discovered spontaneous cation exchange reaction is different from the well-known cation exchange of cation to cation process. It breaks through the limitation that cation exchange reactions must occur in ionic crystals and was employed for tuning of metal nanoparticle compositions, structures, and properties by cation dopant and making SAAs by independent dispersion of cations on nanoparticles using charge–charge repulsion between metal cations. The prepared PdRu and PdCe catalysts exhibited superior performance in the methanol oxidation reaction and hydrogen evolution reaction, in which Pt catalysts are mainly used. These results confirm this cation exchange reaction could be employed as a facile method to prepare various SAAs.

Author Contributions

T. Y., J. P., J. W. H. conceived the project and oversaw all the research phases. T. Y., and X. X. designed the experiments. X. X. fabricated the nanoparticles and performed the electrocatalysis applications. S. K. characterized and analyzed the materials. S. C. and J. W. H. performed theoretical analyses and DFT calculations. T. Y. and X. X. wrote the manuscript. All authors commented on and revised the manuscript.

Conflicts of interest

There are no conflicts to declare.

Acknowledgements

This work was supported by the National Research Foundation of Korea (NRF) grants funded by the Korean government (MSIP) [grant no. (NRF-2021R1A5A6002853 and NRF-2020R1A2C1003885) (T. Y.)]; Institute for Basic Science (IBS-R006-D1) (J. P.); Korea Toray Science Foundation (J. P.); the National Research Foundation of Korea (NRF) [grant no. NRF-2017R1A5A1015365 and NRF-2020R1A2C2101871 (J. P.), and NRF-2021R1A2C3004019 (J. W. H.)].

References

1 Z. Li, M. Saruyama, T. Asaka, Y. Tatetsu and T. Teranishi, *Science*, 2021, **373**, 332–337.
2 X. Li, M. Ji, H. Li, H. Wang, M. Xu, H. Rong, J. Wei, J. Liu, J. Liu and W. Chen, *Matter*, 2020, **2**, 554–586.
3 T. Ling, M. Jaroniec and S. Z. Qiao, *Adv. Mater.*, 2020, **32**, 2001866.
4 T. Holtus, L. Helmbrecht, H. C. Hendrikse, I. Baglai, S. Meuret, G. W. Adhyaksa, E. C. Garnett and W. L. Noorduin, *Nat. Chem.*, 2018, **10**, 740–745.
5 J. Shamsi, A. S. Urban, M. Imran, L. De Trizio and L. Manna, *Chem. Rev.*, 2019, **119**, 3296–3348.
6 Y. Xia, S. Liu, K. Wang, X. Yang, L. Lian, Z. Zhang, J. He, G. Liang, S. Wang and M. Tan, *Adv. Funct. Mater.*, 2020, **30**, 1907379.
7 P. Hao, M. Xie, S. Chen, M. Li, F. Bi, Y. Zhang, M. Lin, X. Guo, W. Ding and X. Guo, *Sci. Adv.*, 2020, **6**, eaay7031.
8 V. Lesnyak, C. George, A. Genovese, M. Prato, A. Casu, S. Ayyappan, A. Scarpellini and L. Manna, *ACS Nano*, 2014, **8**, 8407–8418.
9 X. Cheng, J. Liu, X. Wan, H. Wang, Y. Li, J. Liu, H. Rong, M. Xu, W. Chen and J. Zhang, *Chem. Commun.*, 2018, **54**, 9993–9996.
10 R. Zeng, K. Lian, B. Su, L. Lu, J. Lin, D. Tang, S. Lin and X. Wang, *Angew. Chem., Int. Ed.*, 2021, **60**, 25055–25062.
11 R. Tu, Y. Xie, G. Bertoni, A. Lak, R. Gaspari, A. Rapallo, A. Cavalli, L. De Trizio and L. Manna, *J. Am. Chem. Soc.*, 2016, **138**, 7082–7090.
12 R. D. Robinson, B. Sadtler, D. O. Demchenko, C. K. Erdonmez, L.-W. Wang and A. P. Alivisatos, *Science*, 2007, **317**, 355–358.
13 D. H. Son, S. M. Hughes, Y. Yin and A. Paul Alivisatos, *Science*, 2004, **306**, 1009–1012.
14 H.-L. Wu, R. Sato, A. Yamaguchi, M. Kimura, M. Haruta, H. Kurata and T. Teranishi, *Science*, 2016, **351**, 1306–1310.
15 R. T. Hannagan, G. Giannakakis, M. Flytzani-Stephanopoulos and E. C. H. Sykes, *Chem. Rev.*, 2020, **120**, 12044–12088.
16 R. T. Hannagan, G. Giannakakis, R. Réocreux, J. Schumann, J. Finzel, Y. Wang, A. Michaelides, P. Deshlahra, P. Christopher and M. Flytzani-Stephanopoulos, *Science*, 2021, **372**, 1444–1447.
17 G. Giannakakis, M. Flytzani-Stephanopoulos and E. C. H. Sykes, *Acc. Chem. Res.*, 2018, **52**, 237–247.
18 A. Wang, J. Li and T. Zhang, *Nat. Rev. Chem.*, 2018, **2**, 65–81.
19 M. D. Marcinkowski, M. T. Darby, J. Liu, J. M. Wimble, F. R. Lucci, S. Lee, A. Michaelides, M. Flytzani-Stephanopoulos, M. Stamatakis and E. C. H. Sykes, *Nat. Chem.*, 2018, **10**, 325–332.
20 S. Shao, Y. Yang, K. Sun, S. Yang, A. Li, F. Yang, X. Luo, S. Hao and Y. Ke, *ACS Catal.*, 2021, **11**, 12146–12158.
21 F. Xing, J. Jeon, T. Toyao, K.-i. Shimizu and S. Furukawa, *Chem. Sci.*, 2019, **10**, 8292–8298.
22 G. Sun, Z.-J. Zhao, R. Mu, S. Zha, L. Li, S. Chen, K. Zang, J. Luo, Z. Li and S. C. Purdy, *Nat. Commun.*, 2018, **9**, 4454.
23 X. Xiao, H. Jeong, J. Song, J.-P. Ahn, J. Kim and T. Yu, *Chem. Commun.*, 2019, **55**, 11952–11955.
24 R. A. Carlton, C. E. Lyman and J. E. Roberts, *Scanning*, 2004, **26**, 167–174.
25 G. Kresse and J. Furthmüller, *Phys. Rev. B: Condens. Matter Mater. Phys.*, 1996, **54**, 11169.
26 J. P. Perdew, K. Burke and M. Ernzerhof, *Phys. Rev. Lett.*, 1996, **77**, 3865.
27 H. J. Monkhorst and J. D. Pack, *Phys. Rev. B: Condens. Matter Mater. Phys.*, 1976, **13**, 5188.
28 G. Henkelman and H. Jónsson, *J. Chem. Phys.*, 2000, **113**, 9978–9985.
29 E. Sanville, S. D. Kenny, R. Smith and G. Henkelman, *J. Comput. Chem.*, 2007, **28**, 899–908.
30 J. Rossmeisl, A. Logadottir and J. K. Nørskov, *Chem. Phys.*, 2005, **319**, 178–184.
31 Z. Gu, H. Xu, D. Bin, B. Yan, S. Li, Z. Xiong, K. Zhang and Y. Du, *Colloids Surf., A*, 2017, **529**, 651–658.
32 L. P. A. Guerrero-Ortega, E. Ramirez-Meneses, R. Cabrera-Sierra, L. M. Palacios-Romero, K. Philippot, C. R. Santiago-Ramirez, L. Lartundo-Rojas and A. Manzo-Robledo, *J. Mater. Sci.*, 2019, **54**, 13694–13714.
33 M. Łukaszewski, M. Soszko and A. Czerwiński, *Int. J. Electrochem. Sci.*, 2016, **11**, 4442–4469.
34 W. Sheng, M. Myint, J. G. Chen and Y. Yan, *Energy Environ. Sci.*, 2013, **6**, 1509–1512.
35 X. Y. Song, W. Q. Li, X. J. Liu, Y. S. Wu, D. He, Z. J. Ke, L. Cheng, C. Z. Jiang, G. M. Wang, X. H. Xiao and Y. Li, *J. Energy Chem.*, 2021, **55**, 154–161.
36 A. Griboval-Constant, J.-M. Giraudon, I. Twagishema, G. Leclercq, M. E. Rivas, J. Alvarez, M. Perez-Zurita and M. Goldwasser, *J. Mol. Catal. A: Chem.*, 2006, **259**, 187–196.
37 J. Wojciechowska, E. Gitzhofer, J. Grams, A. M. Ruppert and N. Keller, *Materials*, 2018, **11**, 2329.
38 Z. Feng, X. Chen and X. Bai, *Environ. Sci. Pollut. Res.*, 2021, **28**, 61623–61635.
39 E. A. Paoli, F. Masini, R. Frydendal, D. Deiana, C. Schlaup, M. Malizia, T. W. Hansen, S. Horch, I. E. Stephens and I. Chorkendorff, *Chem. Sci.*, 2015, **6**, 190–196.
40 K. Mech, P. Żabiński, R. Kowalik and K. Fitzner, *J. Electrochem. Soc.*, 2013, **160**, H770.
41 S. Harjanto, Y. Cao, A. Shibayama, I. Naitoh, T. Nanami, K. Kasahara, Y. Okumura, K. Liu and T. Fujita, *Mater. Trans.*, 2006, **47**, 129–135.
42 D. Sil, J. Hines, U. Udeoyo and E. Borguet, *ACS Appl. Mater. Interfaces*, 2015, **7**, 5709–5714.
43 L. K. Xiong, Z. T. Sun, X. Zhang, L. Zhao, P. Huang, X. W. Chen, H. D. Jin, H. Sun, Y. B. Lian, Z. Deng, M. H. Rummerli, W. J. Yin, D. Zhang, S. Wang and Y. Peng, *Nat. Commun.*, 2019, **10**, 3782.
44 Z. C. Cai, M. Kamiko, I. Yamada and S. Yagi, *ACS Appl. Nano Mater.*, 2021, **4**, 1445–1454.
45 Q. Tan, G. Wang, L. Nie, A. Dinse, C. Buda, J. Shabaker and D. E. Resasco, *ACS Catal.*, 2015, **5**, 6271–6283.
46 J. K. Nørskov, T. Bligaard, A. Logadottir, J. Kitchin, J. G. Chen, S. Pandelov and U. Stimming, *J. Electrochem. Soc.*, 2005, **152**, J23.